

HYPERSENSPECTRAL SUPER-RESOLUTION VIA LOW RANK TENSOR TRIPLE DECOMPOSITION

XIAOFEI CUI^{✉1} AND JINGYA CHANG^{✉*1}

¹School of Mathematics and Statistics, Guangdong University of Technology, China

ABSTRACT. Hyperspectral image (HSI) and multispectral image (MSI) fusion aims at producing a super-resolution image (SRI). In this paper, we establish a nonconvex optimization model for image fusion problem through low rank tensor triple decomposition. Using the L-BFGS approach, we develop a first-order optimization algorithm for obtaining the desired super-resolution image (TTDSR). Furthermore, two detailed methods are provided for calculating the gradient of the objective function. With the aid of the Kurdyka-Łojasiewicz property, the iterative sequence is proved to converge to a stationary point. Finally, experimental results on different datasets show the effectiveness of our proposed approach.

1. Introduction. Equipment for hyperspectral imaging uses an unusual sensor to produce images with great spectral resolution. The key factor in an image is the electromagnetic spectrum obtained by sampling at hundreds of continuous wavelength intervals. Because hyperspectral images have hundreds of bands, spectral information is abundant [32]. Hyperspectral images are now the core of a large and increasing number of remote sensing applications, such as environmental monitoring [4, 25], target classification [41, 8] and anomaly detection [7, 37].

With optical sensors, there is a fundamental compromise among spectral resolution, spatial resolution and signal-to-noise ratio. Hyperspectral images therefore have a high spectral resolution but a low spatial resolution. Contrarily, multispectral sensors, which only have a few spectral bands, can produce images with higher spatial resolution but poorer spectral resolution [5].

The approaches for addressing hyperspectral and multispectral images fusion issues can be categorized into four classes [42]. The pan-sharpening approach falls within the first category, which includes component substitution [27, 1] and multi-resolution analysis [6]. Selva [30] and Liu [22] proposed multi-resolution analysis method to extract spatial details that were injected into the interpolated hyperspectral image. Chen et al. [9] divided all bands of the images into several regions and then fused the images of each region by the pan-sharpening approach. Unfortunately, these methods may lead to spectral distortion. The second category is subspace-based formulas. The main idea is to explore the low-dimensional representation of hyperspectral images, which are regarded as a linear combination of a

2020 *Mathematics Subject Classification.* Primary: 90C30, 90C90, 90-08, 90-10, 49M37.

Key words and phrases. Tensor triple decomposition, nonconvex programming, Kurdyka-Łojasiewicz property, image fusion, hyperspectral image, multispectral image.

This work is supported by National Natural Science Foundation of China (grant No. 11901118 and 62073087).

*Corresponding author: Jingya Chang.

set of basis vectors or spectral features [18, 38, 34]. Hardie et al. [15] employed Bayesian formulas to solve the image fusion problem with the maximum posteriori probability. The method based on matrix factorization falls within the third category. Under these circumstances, HSI and MSI are regarded as the degradation versions of the reference SRI. Yokoya et al. [40] proposed a coupled nonnegative matrix factorization method, which estimated the basic vectors and its coefficients blindly and then calculated the endmember matrix and degree matrix by alternating optimization algorithm. In addition, there are methods combining sparse regularization and spatial regularization [19, 31], such as a low rank matrix decomposition model for decomposing a hyperspectral image into a super-resolution image and a difference image in [12, 42].

Tensor decomposition methods fall within the fourth category. Tensor, a higher-order extension of matrix, can capture the correlation between the spatial and spectral domains in hyperspectral images simultaneously. Representing hyperspectral and multispectral images as third-order tensors has been widely used in hyperspectral image denoising and super-resolution problems. The hyperspectral image is a three-dimensional data cube with two spatial dimensions (height and width) and one spectral dimension [17, 33, 23]. The spatial details and spectral structures of the SRI therefore are both more accurate.

By utilizing low rank tensor decomposition technology to explore the low rank properties of hyperspectral images, high spatial resolution and accurate restoration guarantees are obtained. Kanatsoulis et al. [20] proposed treating the super-resolution problem as a coupled tensor approximation, where the super-resolution image satisfied low rank Canonical Polynomial (CP) decomposition. Later, Li et al. [28, 24] considered a novel approach based on tucker decomposition. Xu et al. [39] first considered that the target SRI exhibited both the sparsity and the piecewise smoothness on three modes and then used tucker decomposition to construct model. Dian et al. [13] applied tensor kernel norm to explore low rank property of SRI. He et al. [16] proposed tensor ring decomposition model for addressing the image fusion problem.

In this paper, we propose a novel model based on low rank tensor triple decomposition to address the hyperspectral and multispectral images fusion problem. Triple decomposition breaks down a third-order tensor into three smaller tensors with predetermined dimensions. It is effectively applied in tensor completion and image restoration [29, 11]. The structures of image fusion and triple decomposition are presented in Figure 1. The optimization model is solved by the L-BFGS algorithm. The convergent results are given with the help of Kurdyka-Łojasiewicz property of the objective function. Numerical experiments demonstrate that the proposed TTDSR method performs well and the convergent conclusion is also validated numerically.

The rest of this paper is organized as follows. In section 2, we first provide definitions used in the paper and present the basic algebraic operations of tensors. In section 3, we introduce our motivation and model for the hyperspectral and multispectral images fusion. In section 4, the L-BFGS algorithm and the gradient calculation are also presented in detail. Convergence analysis of the algorithm is available in section 5. In section 6, experimental results on two datasets are given. The conclusion is given in section 7.

2. Preliminary. Let \mathbb{R} be the real field. We use lowercase letters and boldface lowercase letters to represent scalars and vectors respectively, while capital letters and calligraphic letters stand for matrices and tensors respectively.

An m th order n dimensional tensor \mathcal{A} is a multidimensional array with its entry being

$$\mathcal{A}_{i_1, i_2, \dots, i_m} = a_{i_1, i_2, \dots, i_m}, \text{ for } i_j = 1, \dots, n, j = 1, \dots, m.$$

Similarly, the i th entry in a vector \mathbf{a} is symbolized by $(\mathbf{a})_i = a_i$, and the (i, j) th entry of a matrix A is $(A)_{ij} = a_{ij}$. Unless otherwise specified, the order of tensor is set to three hereafter in this paper. Without loss of generality, we denote $\mathcal{A} \in \mathbb{R}^{n_1 \times n_2 \times n_3}$. A fiber of \mathcal{A} is a vector produced by fixing two indices of \mathcal{A} , such as $\mathcal{A}(i, j, :)$ for any $i \in [1, \dots, n_1], j \in [1, \dots, n_2]$. A slice of \mathcal{A} is a matrix by varying two of its indices while fixing another one, such as $\mathcal{A}(:, :, k)$ for any $k \in [1, \dots, n_3]$. The geometric structures of the tensor expansion are shown in Figure 2.

The mode- k product of the tensor \mathcal{A} and a matrix X is an extension of matrix product. Suppose matrices $F \in \mathbb{R}^{l \times n_1}$, $G \in \mathbb{R}^{m \times n_2}$, and $H \in \mathbb{R}^{n \times n_3}$. The mode-1 product of \mathcal{A} and F is denoted as $\mathcal{A} \times_1 F$ with its elements being

$$(\mathcal{A} \times_1 F)_{tjk} = \sum_{i=1}^{n_1} a_{ijk} f_{ti}, \quad \text{for } t = 1, \dots, l, j = 1, \dots, n_2, k = 1, \dots, n_3.$$

Also we have

$$(\mathcal{A} \times_2 G)_{ipk} = \sum_{j=1}^{n_2} a_{ijk} g_{pj}, \quad (\mathcal{A} \times_3 H)_{ijq} = \sum_{k=1}^{n_3} a_{ijk} h_{qk}, \quad (1)$$

for $p = 1, \dots, m, q = 1, \dots, n$. It is easy to verify that

$$\begin{aligned} \mathcal{A} \times_p F \times_q G &= \mathcal{A} \times_q G \times_p F, \quad \forall p, q = 1, 2, 3 \text{ and } p \neq q, \\ \mathcal{A} \times_k F \times_k G &= \mathcal{A} \times_k (GF), \quad \forall k = 1, 2, 3. \end{aligned} \quad (2)$$

The mode- k matricization of \mathcal{A} denoted by $A_{(k)}$ arranges its n_k mode- k fibers as the columns of $A_{(k)}$ in order. The Frobenius norm of tensor \mathcal{A} is given by

$$\|\mathcal{A}\|_F = \left(\sum_{i=1}^{n_1} \sum_{j=1}^{n_2} \sum_{k=1}^{n_3} a_{ijk}^2 \right)^{1/2}. \quad (3)$$

The unfolding related no matter with tensors, matrices or vectors in the following part is carried out under the precondition that the left index varies more rapidly than the right one. Subscript represents dimension. We note that $\text{vec}(B_{m \times n})$ creates a column vector \mathbf{b}_{mn} by stacking the columns of $B_{m \times n}$ below one another, i.e., $(\mathbf{b}_{mn})_{i+(j-1)m} = b_{ij}$. In addition, the kronecker product of matrices $B_{m \times n}$ and $C_{p \times q}$ is

$$B_{m \times n} \otimes C_{p \times q} = \begin{pmatrix} b_{11}C_{p \times q} & b_{12}C_{p \times q} & \cdots & b_{1n}C_{p \times q} \\ b_{21}C_{p \times q} & b_{22}C_{p \times q} & \cdots & b_{2n}C_{p \times q} \\ \cdots & \cdots & \cdots & \cdots \\ b_{m1}C_{p \times q} & b_{m2}C_{p \times q} & \cdots & b_{mn}C_{p \times q} \end{pmatrix},$$

for $s = 1, \dots, p, t = 1, \dots, q$. It generates a large matrix $D_{pm \times qn} = B_{m \times n} \otimes C_{p \times q}$, whose entries are $d_{gh} = b_{ij}c_{st}$ with $g = s + (i-1)p$ and $h = t + (j-1)q$. By this

rule, unfolding matrices of tensor \mathcal{A} could be represented by

$$\begin{aligned} (A_{n_1 \times n_2 n_3})_{i, j+(k-1)n_2} &= a_{ijk}, & (A_{n_1 \times n_3 n_2})_{i, k+(j-1)n_3} &= a_{ijk}, \\ (A_{n_2 \times n_3 n_1})_{j, k+(i-1)n_3} &= a_{ijk}, & (A_{n_2 \times n_1 n_3})_{j, i+(k-1)n_1} &= a_{ijk}, \\ (A_{n_3 \times n_1 n_2})_{k, i+(j-1)n_1} &= a_{ijk}, & (A_{n_3 \times n_2 n_1})_{k, j+(i-1)n_2} &= a_{ijk}. \end{aligned} \quad (4)$$

Moreover, $A_{n_1 n_2 \times n_3} = (A_{n_3 \times n_1 n_2})^\top$.

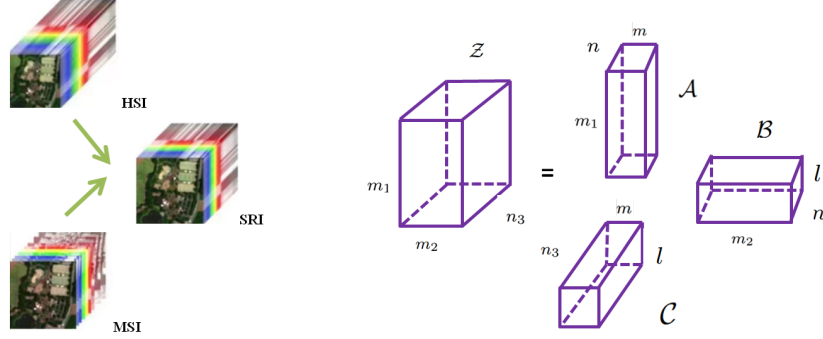


FIGURE 1. The image fusion is displayed in the left image, and the tensor triple decomposition structure is shown in the right.

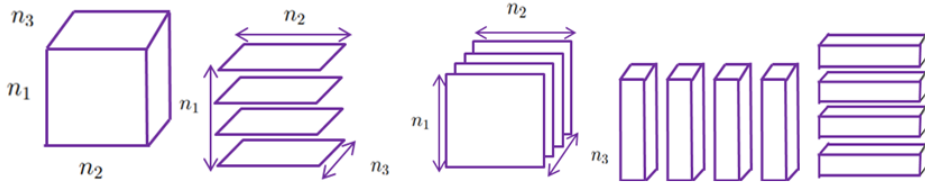


FIGURE 2. Slices and fibers of tensor \mathcal{A} . From left to right are horizontal slices $\mathcal{A}_{i,:,:}$, frontal slices $\mathcal{A}_{:,:,k}$, column fibers $\mathcal{A}_{i,:,k}$, and row fibers $\mathcal{A}_{:,j,k}$.

3. The tensor triple decomposition (TTD) model for HSI-MSI fusion.

Tensors can describe high dimensional relationship. The hyperspectral and multispectral images are naturally third-order tensors. Methods based on low rank matrix decomposition reconstruct the 3-d tensor data into a 2-d matrix data at beginning, which destroy the original 3-d structure and may cause negative influence on the fusion consequences. Therefore, hyperspectral and multispectral image fusion problems have been investigated with the aid of various tensor decompositions in recent years. The tensor triple decomposition model has certain advantages over the classical CP and Tucker decompositions. The triple rank is less than or equal to CP rank, which has been proved theoretically and practically. As described in theorem 2.1 of [29], low rank triple decomposition and triple ranks are well-defined. The proposed triple decomposition has the low rank properties and performs well

in image restoration. When facing large-scale problems, the lower rank indicates that we transform the problem into a lower dimensional subspace, which is relatively easy to solve. Thus, we employ the tensor triple decomposition framework to establish the hyperspectral super-resolution model.

Define $\mathcal{Y}_h \in \mathbb{R}^{n_1 \times n_2 \times n_3}$, $\mathcal{Y}_m \in \mathbb{R}^{m_1 \times m_2 \times m_3}$ and $\mathcal{Z} \in \mathbb{R}^{m_1 \times m_2 \times n_3}$ as hyperspectral image (HSI), multispectral image (MSI) and super-resolution image (SRI) respectively. Here the first two indices n_1 and n_2 or m_1 and m_2 denote the spatial dimensions. The third index n_3 or m_3 indicate the number of spectral bands. Usually, the MSI contains more spatial information than the HSI, that is $m_1 \gg n_1, m_2 \gg n_2$. The HSI has more spectral bands than MSI, which means $n_3 \gg m_3$. Our target is to find the SRI that possesses the high spectral resolution of HSI and the spatial resolution of the MSI, i.e. a super-resolution image.

3.1. The links among SRI, HSI and MSI. Let the mode-3 matricization of \mathcal{Y}_h , \mathcal{Y}_m and \mathcal{Z} be $(Y_h)_{(3)} \in \mathbb{R}^{n_1 n_2 \times n_3}$, $(Y_m)_{(3)} \in \mathbb{R}^{m_1 m_2 \times m_3}$ and $Z_{(3)} \in \mathbb{R}^{m_1 m_2 \times n_3}$. The key point which helps us to construct the relationship among SRI, HSI and MSI is that there exist two linear operators $P_h \in \mathbb{R}^{n_1 n_2 \times m_1 m_2}$ and $P_3 \in \mathbb{R}^{m_3 \times n_3}$ such that $(Y_h)_{(3)} = P_h Z_{(3)}$ and $(Y_m)_{(3)} = Z_{(3)} P_3^T$ [20]. Thus we have

$$\mathcal{Y}_h(:, :, k) = P_1 \mathcal{Z}(:, :, k) P_2^T, \quad \text{for } k = 1, \dots, n_3, \quad (5)$$

where $P_1 \in \mathbb{R}^{n_1 \times m_1}$, $P_2 \in \mathbb{R}^{n_2 \times m_2}$ and $P_2 \otimes P_1 = P_h$. We also have

$$\mathcal{Y}_m(i, j, :) = P_3 \mathcal{Z}(i, j, :), \quad \text{for } i = 1, \dots, m_1, j = 1, \dots, m_2, \quad (6)$$

where $\mathcal{Z}(i, j, :) \in \mathbb{R}^{n_3}$ represents a fiber of \mathcal{Z} and $\mathcal{Y}_m(i, j, :) \in \mathbb{R}^{m_3}$ is a fiber of \mathcal{Y}_m respectively. Therefore, $\mathcal{Y}_h, \mathcal{Y}_m$ can be rewritten as

$$\mathcal{Y}_h = \mathcal{Z} \times_1 P_1 \times_2 P_2, \quad \mathcal{Y}_m = \mathcal{Z} \times_3 P_3. \quad (7)$$

Equations (5) and (6) also are known as the spatial and spectral degradation processes of \mathcal{Z} . The matrices P_1, P_2 respectively describe the downsampling and blurring of the spatial degradation process. Downsampling is considered as linear compression, while blurring describes a linear mixing of neighbouring pixels under a specific kernel in both the row and column dimensions. The matrix P_3 is usually modeled as a band-selection matrix that selects the common spectral bands of the SRI and MSI.

Based on the correlation of spatial and spectral information in hyperspectral and multispectral images, various low rank tensor decomposition models are established to study the problem. For example, suppose \mathcal{Z} is decomposed by Canonical Polyadic decomposition into the sum of several rank-1 tensors, which is represented as $\mathcal{Z} = \llbracket A, B, C \rrbracket$. The HSI-MSI fusion model [20] is denoted as $\mathcal{Y}_h = \llbracket P_1 A, P_2 B, C \rrbracket$ and $\mathcal{Y}_m = \llbracket A, B, P_3 C \rrbracket$. Besides, tucker decomposition is considered [28, 44] and it is expressed as $\mathcal{Y}_h = \mathcal{C} \times_1 (P_1 A) \times_2 (P_2 B) \times_3 C$ and $\mathcal{Y}_m = \mathcal{C} \times_1 A \times_2 B \times_3 (P_3 C)$.

3.2. The new model for HSI-MSI fusion. In [29], Qi et al. proposed a new tensor decomposition, named tensor triple decomposition, which can effectively express the original tensor information by three low rank tensors. Therefore, we establish the hyperspectral and multispectral image fusion model by low rank tensor triple decomposition.

First, we introduce the tensor triple decomposition in detail. Tensor triple decomposition of a third-order $\mathcal{Z} \in \mathbb{R}^{m_1 \times m_2 \times n_3}$ representing the target SRI takes the following form

$$\mathcal{Z} = ABC, \quad (8)$$

where $\mathcal{A} \in \mathbb{R}^{m_1 \times m \times n}$, $\mathcal{B} \in \mathbb{R}^{l \times m_2 \times n}$ and $\mathcal{C} \in \mathbb{R}^{l \times m \times n_3}$. It can also be denoted as $\mathcal{Z} = \llbracket \mathcal{A}, \mathcal{B}, \mathcal{C} \rrbracket$ with its entries

$$(\llbracket \mathcal{A}, \mathcal{B}, \mathcal{C} \rrbracket)_{ijk} = \sum_{t=1}^l \sum_{p=1}^m \sum_{q=1}^n a_{ipq} b_{tjq} c_{tpk}, \quad (9)$$

for $i = 1, \dots, m_1$, $j = 1, \dots, m_2$, and $k = 1, \dots, n_3$. The smallest value of r such that (9) holds is called the triple rank of \mathcal{Z} and denoted as $\text{rank}(\mathcal{Z}) = r$. If $l = m = n = r$, equation (8) is called low rank triple decomposition of \mathcal{Z} , where $r \leq \text{mid}\{m_1, m_2, n_3\}$ and mid represents the larger number in the middle [29, 11]. In particular, according to [11, Theorem 2.2], triple decomposition satisfies the following equations

$$\begin{aligned} Z_{m_1 \times m_2 n_3} &= A_{m_1 \times n m} (E_m \otimes B_{n \times m_2 l}) (C_{l m \times n_3} \otimes E_{m_2}), \\ Z_{m_2 \times n_3 m_1} &= B_{m_2 \times l n} (E_n \otimes C_{l \times n_3 m}) (A_{m n \times m_1} \otimes E_{n_3}), \\ Z_{n_3 \times m_2 m_1} &= C_{n_3 \times l m} (E_m \otimes B_{l \times m_2 n}) (A_{n m \times m_1} \otimes E_{m_2}), \end{aligned} \quad (10)$$

where E is an identity matrix with a proper size.

Next, we propose a new model with the help of low rank tensor triple decomposition. Assume \mathcal{A} , \mathcal{B} and \mathcal{C} are the low rank triple decomposition tensors of tensor \mathcal{Z} . For the connection (7), we have

$$\mathcal{Y}_h = \llbracket \mathcal{A} \times_1 P_1, \mathcal{B} \times_2 P_2, \mathcal{C} \rrbracket \quad \text{and} \quad \mathcal{Y}_m = \llbracket \mathcal{A}, \mathcal{B}, \mathcal{C} \times_3 P_3 \rrbracket. \quad (11)$$

Since the best low rank approximation problem of tensors may be ill-posed, we add the Tikhonov regularization term and get the following optimization model

$$\begin{aligned} \min_{\mathcal{A}, \mathcal{B}, \mathcal{C}} f(\mathcal{A}, \mathcal{B}, \mathcal{C}) &:= \|\mathcal{Y}_h - \llbracket \mathcal{A} \times_1 P_1, \mathcal{B} \times_2 P_2, \mathcal{C} \rrbracket\|_F^2 + \|\mathcal{Y}_m - \llbracket \mathcal{A}, \mathcal{B}, \mathcal{C} \times_3 P_3 \rrbracket\|_F^2 \\ &+ \mu (\|\mathcal{A}\|_F^2 + \|\mathcal{B}\|_F^2 + \|\mathcal{C}\|_F^2), \end{aligned} \quad (12)$$

where μ is regularization parameter. Thus, we employ the optimization model (12) to obtain the triple decomposition tensors \mathcal{A} , \mathcal{B} and \mathcal{C} , and to produce the super-resolution image SRI by $\mathcal{Z} = \llbracket \mathcal{A}, \mathcal{B}, \mathcal{C} \rrbracket$.

4. The L-BFGS algorithm for solving the model. In this section, we focus on numerical approaches for computing a first-order stationary point of the optimization problem (12). Since the limited memory BFGS (L-BFGS) algorithm [21] is powerful for large scale nonlinear unconstrained optimization, we apply it to produce a search direction and consider using inexact line search techniques to update the iteration step size. In the computaion process, we either matricize or vectorize the tensor variable to get the gradient of the objective function. For convenience, we demonstrate the algorithm and its convergence analysis for

$$\mathbf{x} := \begin{pmatrix} \mathbf{a}_{m_1 r r} \\ \mathbf{b}_{m_2 r r} \\ \mathbf{c}_{n_3 r r} \end{pmatrix} = \begin{pmatrix} A_{m_1 r r \times 1} \\ B_{m_2 r r \times 1} \\ C_{n_3 r r \times 1} \end{pmatrix}. \quad (13)$$

4.1. Limited memory BFGS algorithm. BFGS is a quasi-Newton method which updates the approximation of the inverse of a Hessian iteratively. In the current iteration k , it constructs an approximation matrix H_k to estimate the inverse of

Hessian of $f(\mathbf{x})$. The gradient of $f(\mathbf{x})$ is defined as $\mathbf{g}(\mathbf{x})$. At the beginning, we introduce the basic BFGS update. Let

$$\mathbf{y}_k = \nabla f(\mathbf{x}_{k+1}) - \nabla f(\mathbf{x}_k), \quad \mathbf{s}_k = \mathbf{x}_{k+1} - \mathbf{x}_k, \quad V_k = I - \rho_k \mathbf{y}_k \mathbf{s}_k^\top, \quad (14)$$

and

$$\rho_k = \begin{cases} \frac{1}{\mathbf{y}_k^\top \mathbf{s}_k}, & \text{if } \mathbf{y}_k^\top \mathbf{s}_k \geq \epsilon \\ 0, & \text{otherwise} \end{cases}, \quad (15)$$

where I is an identity matrix, \top represents transposition and $\epsilon \in (0, 1)$ is a small positive constant. The matrix H_k is updated by

$$H_{k+1} = V_k^\top H_k V_k + \rho_k \mathbf{s}_k \mathbf{s}_k^\top. \quad (16)$$

To deal with large-scale optimization problems, Liu and Nocedal [21] proposed the L-BFGS algorithm that implemented BFGS in an economical manner. Given a constant l . When $k \geq l$, only information of l matrices $H_{k-1}, H_{k-2}, \dots, H_{k-l}$ are used to calculate the matrix H_k by the following recursive form

$$H_k = V_{k-m}^\top H_{k-m} V_{k-m} + \rho_{k-m} \mathbf{s}_{k-m} \mathbf{s}_{k-m}^\top, \quad \text{for } m = 1, 2, \dots, l. \quad (17)$$

In order to save memory, the initial matrix H_{k-l} is replaced by

$$H_k^{(0)} = \gamma_k I. \quad (18)$$

Here $\gamma_k > 0$ is usually determined by the Barzilai-Borwein method [3] as follows

$$\gamma_k^{\text{BB1}} = \frac{\mathbf{y}_k^\top \mathbf{s}_k}{\|\mathbf{y}_k\|^2} \quad \text{and} \quad \gamma_k^{\text{BB2}} = \frac{\|\mathbf{s}_k\|^2}{\mathbf{y}_k^\top \mathbf{s}_k}. \quad (19)$$

If $l \geq k$, H_k is generated by the traditional BFGS method. The L-BFGS method can be implemented in an inexpensive two-loop recursion way which is shown in Algorithm 1.

The $\mathbf{p}_k = -H_k \mathbf{g}(\mathbf{x}_k)$ generated by L-BFGS is a gradient-related descent direction for H_k being a positive definite matrix, where the proof process is presented in Lemma B.2. Then we find a proper step size along the direction \mathbf{p}_k that satisfies the Armijo condition. The computation method for the model (12) is obtained and we demonstrate it in Algorithm 2.

Algorithm 1 The two-loop recursion for L-BFGS [10, 21].

- 1: $\mathbf{q} \leftarrow -\mathbf{g}(\mathbf{x}_k)$
 - 2: **for** $i = k-1, k-2, \dots, k-l$ **do**
 - 3: $\alpha_i \leftarrow \rho_i \mathbf{s}_i^\top \mathbf{q}$
 - 4: $\mathbf{q} \leftarrow \mathbf{q} - \alpha_i \mathbf{y}_i$
 - 5: **end for**
 - 6: **for** $i = k-l, k-l+1, \dots, k-1$ **do**
 - 7: $\beta \leftarrow \rho_i \mathbf{y}_i^\top \mathbf{p}$
 - 8: $\mathbf{p} \leftarrow \mathbf{p} + \mathbf{s}_i (\alpha_i - \beta)$
 - 9: **end for**
 - 10: Stop with result $\mathbf{p} = -H_k \mathbf{g}(\mathbf{x}_k)$.
-

Algorithm 2 Low rank triple decomposition for obtaining super-resolution image (TTDSR).

- 1: Choose constant r and an initial iterate $\mathbf{x}_0 \in \mathbb{R}^{m_1 r r + m_2 r r + n_3 r r}$. Select parameters $l > 0$, $\beta \in (0, 1)$, and $\sigma \in (0, 1)$. Compute $f_0 = f(\mathbf{x}_0)$ and $\mathbf{g}_0 = \nabla f(\mathbf{x}_0)$. Set $k \leftarrow 0$.
 - 2: **while** the sequence of iterates does not converge **do**
 - 3: Generate $\mathbf{p}_k = -H_k \mathbf{g}(\mathbf{x}_k)$ by Algorithm 1.
 - 4: Choose the smallest nonnegative integer ω such that the step size $\alpha = \beta^\omega$ satisfies

$$f(\mathbf{x}_k + \alpha \mathbf{p}_k) \leq f(\mathbf{x}_k) + \sigma \alpha \mathbf{p}_k^\top \mathbf{g}_k. \quad (20)$$
 - 5: Let $\alpha_k = \beta^\omega$ and update the new iterate $\mathbf{x}_{k+1} = \mathbf{x}_k + \alpha_k \mathbf{p}_k$.
 - 6: Compute $f_{k+1} = f(\mathbf{x}_{k+1})$ and $\mathbf{g}_{k+1} = \nabla f(\mathbf{x}_{k+1})$.
 - 7: Compute \mathbf{y}_k , \mathbf{s}_k and ρ_k by (14) and (15), respectively.
 - 8: $k \leftarrow k + 1$.
 - 9: **end while**
-

4.2. Gradient calculation. At each iteration in Algorithm 2, we need to compute the gradient of the objective function. The gradient can be calculated via reshaping the tensor variable into vector or matrix form. For small scale problems, the gradient is easier to obtain when the the tensor variable is turned into a vector than into a matrix, while for large scale problems, the gradient in vector form always leads to insufficient memory in the computation process. In this subsection, we derive the matrix form of the gradient and the vector form ∇f is given in the Appendix A.

Denote $\mathcal{H} = \mathcal{A} \times_1 P_1 \in \mathbb{R}^{n_1 \times m \times n}$, $\mathcal{K} = \mathcal{B} \times_2 P_2 \in \mathbb{R}^{l \times n_2 \times n}$, and $\mathcal{G} = \mathcal{C} \times_3 P_3 \in \mathbb{R}^{l \times m \times m_3}$. According to (10) and (11), we get the following equations

$$(Y_h)_{n_1 \times n_2 n_3} = P_{n_1 \times m_1} A_{m_1 \times nm} (E_m \otimes K_{n \times n_2 l}) (C_{lm \times n_3} \otimes E_{n_2}), \quad (21)$$

$$(Y_h)_{n_2 \times n_3 n_1} = P_{n_2 \times m_2} B_{m_2 \times ln} (E_n \otimes C_{l \times n_3 m}) (H_{mn \times n_1} \otimes E_{n_3}), \quad (22)$$

$$(Y_h)_{n_3 \times n_2 n_1} = C_{n_3 \times lm} (E_m \otimes K_{l \times n_2 n}) (H_{nm \times n_1} \otimes E_{n_2}), \quad (23)$$

$$(Y_m)_{m_1 \times m_2 m_3} = A_{m_1 \times nm} (E_m \otimes B_{n \times m_2 l}) (G_{lm \times m_3} \otimes E_{m_2}), \quad (24)$$

$$(Y_m)_{m_2 \times m_3 m_1} = B_{m_2 \times ln} (E_n \otimes G_{l \times m_3 m}) (A_{mn \times m_1} \otimes E_{m_3}), \quad (25)$$

$$(Y_m)_{m_3 \times m_2 m_1} = P_{m_3 \times n_3} C_{n_3 \times lm} (E_m \otimes B_{l \times m_2 n}) (A_{nm \times m_1} \otimes E_{m_2}). \quad (26)$$

Define $P_2 B_{m_2 \times ln} = K_{n_2 \times ln}$ and $P_3 C_{n_3 \times lm} = G_{m_3 \times lm}$. The function $f(\mathbf{x})$ in (12) is transformed into the objective function of matrix variables $A_{m_1 \times nm}$, $B_{m_2 \times ln}$ and $C_{n_3 \times lm}$ as follows

$$\begin{aligned} f(A, B, C) &= \|P_1 A_{m_1 \times nm} (E_m \otimes K_{n \times n_2 l}) (C_{n_3 \times lm}^T \otimes E_{n_2}) - (Y_h)_{n_1 \times n_2 n_3}\|_F^2 \\ &\quad + \|A_{m_1 \times nm} (E_m \otimes B_{n \times m_2 l}) \left((P_3 C_{n_3 \times lm})^T \otimes E_{m_2} \right) - (Y_m)_{m_1 \times m_2 m_3}\|_F^2 \\ &\quad + \mu \left(\|A_{m_1 \times nm}\|_F^2 + \|B_{m_2 \times ln}\|_F^2 + \|C_{n_3 \times lm}\|_F^2 \right), \end{aligned} \quad (27)$$

$$\begin{aligned}
f(A, B, C) = & \left\| P_2 B_{m_2 \times l n} (E_n \otimes C_{l \times n_3 m}) \left((P_1 A_{m_1 \times m n})^T \otimes E_{n_3} \right) - (Y_h)_{n_2 \times n_3 n_1} \right\|_F^2 \\
& + \left\| B_{m_2 \times l n} (E_n \otimes G_{l \times m_3 m}) \left((A_{m_1 \times m n})^T \otimes E_{m_3} \right) - (Y_m)_{m_2 \times m_3 m_1} \right\|_F^2 \\
& + \mu \left(\|A_{m_1 \times n m}\|_F^2 + \|B_{m_2 \times l n}\|_F^2 + \|C_{n_3 \times l m}\|_F^2 \right),
\end{aligned} \tag{28}$$

$$\begin{aligned}
f(A, B, C) = & \left\| C_{n_3 \times l m} (E_m \otimes K_{l \times n_2 n}) \left((P_1 A_{m_1 \times m n})^T \otimes E_{n_2} \right) - (Y_h)_{n_3 \times n_2 n_1} \right\|_F^2 \\
& + \left\| P_3 C_{n_3 \times l m} (E_m \otimes B_{l \times m_2 n}) \left((A_{m_1 \times n m})^T \otimes E_{m_2} \right) - (Y_m)_{m_3 \times m_2 m_1} \right\|_F^2 \\
& + \mu \left(\|A_{m_1 \times n m}\|_F^2 + \|B_{m_2 \times l n}\|_F^2 + \|C_{n_3 \times l m}\|_F^2 \right).
\end{aligned} \tag{29}$$

For any matrix X , we have $\|X\|_F^2 = \text{tr}(X^T X)$. Therefore we review the derivatives of some useful trace functions with respect to X :

$$\begin{aligned}
\frac{\partial \text{tr}(A X B X^T C)}{\partial X} &= A^T C^T X B^T + C A X B, & \frac{\partial \text{tr}(A X^T B)}{\partial X} &= B A, \\
\frac{\partial \text{tr}(A B A^T)}{\partial A} &= A(B + B^T), & \frac{\partial \text{tr}(B A^T)}{\partial A} &= B, \\
\frac{\partial \text{tr}(A X B)}{\partial X} &= A^T B^T, & \frac{\partial \text{tr}(A B)}{\partial A} &= B^T.
\end{aligned} \tag{30}$$

For simplicity, we denote

$$\begin{aligned}
E_1 &= (E_m \otimes B_{n \times m_2 l}) \left((P_3 C_{n_3 \times l m})^T \otimes E_{m_2} \right), & D_1 &= (E_m \otimes K_{n \times n_2 l}) (C_{n_3 \times l m}^T \otimes E_{n_2}), \\
F_1 &= (E_n \otimes C_{l \times n_3 m}) \left((P_1 A_{m_1 \times m n})^T \otimes E_{n_3} \right), & G_1 &= (E_n \otimes G_{l \times m_3 m}) (A_{m_1 \times m n}^T \otimes E_{m_3}), \\
H_1 &= (E_m \otimes K_{l \times n_2 n}) \left((P_1 A_{m_1 \times m n})^T \otimes E_{n_2} \right), & K_1 &= (E_m \otimes B_{l \times m_2 n}) (A_{m_1 \times n m}^T \otimes E_{m_2}).
\end{aligned}$$

Thus, the partial derivatives with respect to A , B , and C are

$$\begin{aligned}
\frac{\partial f(A, B, C)}{\partial A} &= \frac{\partial \left(\|P_1 A D_1 - Y_h\|_F^2 + \|A E_1 - Y_m\|_F^2 + \mu \left(\|A\|_F^2 + \|B\|_F^2 + \|C\|_F^2 \right) \right)}{\partial A} \\
&= \frac{\partial \text{tr}(\langle P_1 A D_1 - Y_h, P_1 A D_1 - Y_h \rangle + \langle A E_1 - Y_m, A E_1 - Y_m \rangle)}{\partial A} + 2\mu A \\
&= \frac{\partial \text{tr} (P_1 A D_1 D_1^T A^T P_1^T - P_1 A D_1 Y_h^T - Y_h D_1^T A^T P_1^T - Y_h Y_h^T)}{\partial A} \\
&\quad + \frac{\partial \text{tr} (A E_1 E_1^T A^T - A E_1 Y_m^T - Y_m E_1^T A^T + Y_m^T Y_m)}{\partial A} + 2\mu A \\
&= 2 \left(P_1^T P_1 A D_1 D_1^T - P_1^T Y_h D_1^T + A E_1 E_1^T - Y_m E_1^T + \mu A \right),
\end{aligned} \tag{31}$$

$$\begin{aligned}
\frac{\partial f(A, B, C)}{\partial B} &= \frac{\partial \left(\|P_2 B F_1 - Y_h\|_F^2 + \|B G_1 - Y_m\|_F^2 + \mu \left(\|A\|_F^2 + \|B\|_F^2 + \|C\|_F^2 \right) \right)}{\partial B} \\
&= \frac{\partial \text{tr} \left(\langle P_2 B F_1 - Y_h, P_2 B F_1 - Y_h \rangle + \langle B G_1 - Y_m, B G_1 - Y_m \rangle \right)}{\partial B} + 2\mu B \\
&= \frac{\partial \text{tr} \left(P_2 B F_1 F_1^T B^T P_2^T - P_2 B F_1 Y_h^T - Y_h F_1^T B^T P_2^T - Y_h Y_h^T \right)}{\partial B} \\
&\quad + \frac{\partial \text{tr} \left(B G_1 G_1^T B^T - B G_1 Y_m^T - Y_m G_1^T B^T + Y_m^T Y_m \right)}{\partial B} + 2\mu B \\
&= 2 \left(P_2^T P_2 B F_1 F_1^T - P_2^T Y_h F_1^T + B G_1 G_1^T - Y_m G_1^T + \mu B \right), \tag{32}
\end{aligned}$$

$$\begin{aligned}
\frac{\partial f(A, B, C)}{\partial C} &= \frac{\partial \left(\|C H_1 - Y_h\|_F^2 + \|P_3 C K_1 - Y_m\|_F^2 + \mu \left(\|A\|_F^2 + \|B\|_F^2 + \|C\|_F^2 \right) \right)}{\partial C} \\
&= \frac{\partial \text{tr} \left(\langle C H_1 - Y_h, C H_1 - Y_h \rangle + \langle P_3 C K_1 - Y_m, P_3 C K_1 - Y_m \rangle \right)}{\partial C} + 2\mu C \\
&= \frac{\partial \text{tr} \left(C H_1 H_1^T C^T - C H_1 Y_h^T - Y_h H_1^T C^T + Y_h^T Y_h \right)}{\partial C} \\
&\quad + \frac{\partial \text{tr} \left(P_3 C K_1 K_1^T C^T P_3^T - P_3 C K_1 Y_m^T - Y_m K_1^T C^T P_3^T - Y_m Y_m^T \right)}{\partial C} + 2\mu C \\
&= 2 \left(C H_1 H_1^T - Y_h H_1^T + P_3^T P_3 C K_1 K_1^T - P_3^T Y_m K_1^T + \mu C \right). \tag{33}
\end{aligned}$$

5. Convergence analysis. In this section, we analyze the convergence of $\|\mathbf{g}(\mathbf{x})\|$ and show that our proposed method produces a globally convergent iteration.

Lemma 5.1. *There exists a positive number M such that*

$$|f(\mathbf{x})| \leq M, \|\mathbf{g}(\mathbf{x})\| \leq M, \|H(\mathbf{x})\| \leq M. \tag{34}$$

Proof. Because $\mathbf{p}_k = -H_k \mathbf{g}(\mathbf{x}_k)$ generated by L-BFGS is a gradient-related descent direction. There exists a positive number satisfies the Armijo condition in (20) and the sequence of objective function value $\{f(\mathbf{x}_k)\}$ decreases monotonically. Since the value of the objective function $f(\mathbf{x})$ in (12) is nonnegative, $f(\mathbf{x})$ is bounded, i.e. $0 \leq f(\mathbf{x}) \leq M$ holds.

The regularization term $\mu (\|\mathcal{A}\|_F^2 + \|\mathcal{B}\|_F^2 + \|\mathcal{C}\|_F^2)$ in the objective function indicates that the sequence $\{\mathbf{x}_k\}$ is bounded. Because $\mathbf{g}(\mathbf{x})$ is a linear function of \mathbf{x} , $\|\mathbf{g}(\mathbf{x})\|$ is also bounded. The proof of the boundedness of $H(\mathbf{x})$ is shown in Appendix B. Thus, we get Lemma 5.1. \square

Furthermore, we have the following Lemma 5.2.

Lemma 5.2. *There exist constants C_m and C_M satisfy $0 < C_m \leq 1 \leq C_M$,*

$$\mathbf{p}_k^\top \mathbf{g}(\mathbf{x}_k) \leq -C_m \|\mathbf{g}(\mathbf{x}_k)\|^2 \quad \text{and} \quad \|\mathbf{p}_k\| \leq C_M \|\mathbf{g}(\mathbf{x}_k)\|. \tag{35}$$

Proof. The proof can be found in the Appendix B. \square

Because of boundedness and monotonicity of $\{f(\mathbf{x}_k)\}$, the sequence of function value converges. The conclusion is given in Theorem 5.3.

Theorem 5.3. *Assume that Algorithm 2 generates an infinite sequence of function values $\{f(\mathbf{x}_k)\}$. Then, there exists a constant f_* such that*

$$\lim_{k \rightarrow \infty} f(\mathbf{x}_k) = f_*. \tag{36}$$

Next, we prove that every accumulation point of iterates $\{\mathbf{x}_k\}$ is a first-order stationary point. At last, by utilizing the Kurdyka-Łojasiewicz property [2], we show that the sequence of iterates $\{\mathbf{x}_k\}$ is also convergent. The following lemma means that the step size is lower bounded.

Lemma 5.4. *There exists a constant $\alpha_{\min} > 0$ such that*

$$\alpha_k \geq \alpha_{\min} > 0, \quad \forall k \in \mathbf{N}^+. \quad (37)$$

Proof. Let $0 < \alpha \leq \tilde{\alpha} = \frac{(1-\sigma)C_m}{\frac{1}{2}MC_M^2}$. From Lemma 5.2, for $\alpha \in (0, \tilde{\alpha}]$, it yields that

$$\begin{aligned} \alpha \mathbf{p}_k^T \mathbf{g}_k + \frac{1}{2} M \alpha^2 \|\mathbf{p}_k\|^2 - \sigma \alpha \mathbf{p}_k^T \mathbf{g}_k &= (1-\sigma) \alpha \mathbf{p}_k^T \mathbf{g}_k + \frac{1}{2} M \alpha^2 \|\mathbf{p}_k\|^2 \\ &\leq (1-\sigma) \alpha (-C_m \|\mathbf{g}(\mathbf{x}_k)\|^2) + \frac{1}{2} M \alpha^2 C_M^2 \|\mathbf{g}_k\|^2 \\ &\leq 0. \end{aligned} \quad (38)$$

From Taylor's mean value theorem and $\mathbf{x}_{k+1}(\alpha) = \mathbf{x}_k + \alpha \mathbf{p}_k$, we have

$$\begin{aligned} f(\mathbf{x}_{k+1}(\alpha)) - f(\mathbf{x}_k) &\leq \mathbf{g}_k^T (\mathbf{x}_{k+1}(\alpha) - \mathbf{x}_k) + \frac{1}{2} M \|\mathbf{x}_{k+1}(\alpha) - \mathbf{x}_k\|^2 \\ &= \alpha \mathbf{p}_k^T \mathbf{g}_k + \frac{1}{2} M \alpha^2 \|\mathbf{p}_k\|^2 \\ &\leq \sigma \alpha \mathbf{p}_k^T \mathbf{g}_k, \end{aligned} \quad (39)$$

where the last inequality is valid owing to (38). The rule of inexact line search indicates $\alpha_k \geq \alpha_{\min} = \tilde{\alpha} \beta$. Hence, we find out a lower bound on the step size α . \square

The following theorem proves that every accumulation point of iterates $\{\mathbf{x}_k\}$ is a first-order stationary point.

Theorem 5.5. *Suppose that Algorithm 2 generates an infinite sequence of iterates $\{\mathbf{x}_k\}$. Then,*

$$\lim_{k \rightarrow \infty} \|\mathbf{g}(\mathbf{x}_k)\| = 0. \quad (40)$$

Proof. From Lemma 5.2 and (20), we get

$$f(\mathbf{x}_k) - f(\mathbf{x}_{k+1}) \geq -\sigma \alpha_k \mathbf{p}_k^T \mathbf{g}(\mathbf{x}_k) \geq \sigma \alpha_k C_m \|\mathbf{g}(\mathbf{x}_k)\|^2. \quad (41)$$

The functional series $\sum_{k=1}^{\infty} [f(\mathbf{x}_k) - f(\mathbf{x}_{k+1})]$ satisfies

$$\begin{aligned} 2M \geq f(\mathbf{x}_1) - f_* &= \sum_{k=1}^{\infty} [f(\mathbf{x}_k) - f(\mathbf{x}_{k+1})] \\ &\geq \sum_{k=1}^{\infty} \sigma \alpha_k C_m \|\mathbf{g}(\mathbf{x}_k)\|^2 \\ &\geq \sum_{k=1}^{\infty} \sigma \alpha_{\min} C_m \|\mathbf{g}(\mathbf{x}_k)\|^2. \end{aligned} \quad (42)$$

That is to say,

$$\sum_{k=1}^{\infty} \|\mathbf{g}(\mathbf{x}_k)\|^2 \leq \frac{2M}{\sigma \alpha_{\min} C_m} < +\infty. \quad (43)$$

Hence, $\|\mathbf{g}(\mathbf{x}_k)\|$ converges to zero. \square

Analysis of proximal methods for nonconvex and nonsmooth optimization frequently uses the Kurdyka-Lojasiewicz (KL) property [2]. Since the objective function $f(\mathbf{x})$ is a polynomial and the KL property below holds, we use the KL property to prove the convergence of algorithm.

Proposition 5.6. (*Kurdyka-Lojasiewicz (KL) property*) *Suppose that \mathbf{x}_* is a stationary point of $f(\mathbf{x})$. There is a neighborhood \mathcal{U} of \mathbf{x}_* , an exponent $\theta \in [0, 1)$ and a positive constant K such that for all $\mathbf{x} \in \mathcal{U}$, the following inequality holds:*

$$|f(\mathbf{x}) - f(\mathbf{x}_*)|^\theta \leq K \|\mathbf{g}(\mathbf{x})\|. \quad (44)$$

In particular, we define $0^0 \equiv 0$.

Lemma 5.7. *Suppose that \mathbf{x}_* is a stationary point of $f(\mathbf{x})$ and $\mathcal{A}(\mathbf{x}_*, \delta) = \{\mathbf{x} \in \mathbb{R}^n : \|\mathbf{x} - \mathbf{x}_*\| \leq \delta\} \subseteq \mathcal{U}$ is a neighborhood of \mathbf{x}_* . Let \mathbf{x}_1 be an initial point satisfying*

$$\delta > \frac{C_M K}{\sigma C_m (1 - \theta)} |f(\mathbf{x}_1) - f(\mathbf{x}_*)|^{1-\theta} + \|\mathbf{x}_1 - \mathbf{x}_*\|. \quad (45)$$

Then, the following assertions hold:

$$\mathbf{x}_k \in \mathcal{A}(\mathbf{x}_*, \delta), \quad k = 1, 2, \dots \quad (46)$$

and

$$\sum_{k=1}^{\infty} \|\mathbf{x}_{k+1} - \mathbf{x}_k\| \leq \frac{C_M K}{\sigma C_m (1 - \theta)} |f(\mathbf{x}_1) - f(\mathbf{x}_*)|^{1-\theta}. \quad (47)$$

Proof. The theorem is proved by induction. Obviously, $\mathbf{x}_1 \in \mathcal{A}(\mathbf{x}_*, \delta)$. Now, we assume $\mathbf{x}_i \in \mathcal{A}(\mathbf{x}_*, \delta)$ for all $i = 1, \dots, k$ and KL property holds at these points. Define a concave function

$$\phi(q) \equiv \frac{K}{1 - \theta} |q - f(\mathbf{x}_*)|^{1-\theta} \quad \text{and} \quad q > f(\mathbf{x}_*). \quad (48)$$

Its derivative function is

$$\phi'(q) = \frac{K}{|q - f(\mathbf{x}_*)|^\theta}. \quad (49)$$

For $i = 1, \dots, k$, the first-order condition of the concave function $\phi'(q)$ at $f(\mathbf{x}_i)$ is

$$\begin{aligned} \phi(f(\mathbf{x}_i)) - \phi(f(\mathbf{x}_{i+1})) &\geq \phi'(f(\mathbf{x}_i)) (f(\mathbf{x}_i) - f(\mathbf{x}_{i+1})) \\ &= \frac{K}{|f(\mathbf{x}_i) - f(\mathbf{x}_*)|^\theta} (f(\mathbf{x}_i) - f(\mathbf{x}_{i+1})). \end{aligned} \quad (50)$$

The equation (50) and KL property mean

$$\phi(f(\mathbf{x}_i)) - \phi(f(\mathbf{x}_{i+1})) \geq \frac{1}{\|\mathbf{g}(\mathbf{x}_i)\|} (f(\mathbf{x}_i) - f(\mathbf{x}_{i+1})). \quad (51)$$

By Lemma 5.2 and (41), we have

$$\phi(f(\mathbf{x}_i)) - \phi(f(\mathbf{x}_{i+1})) \geq \sigma \alpha_i C_m \|\mathbf{g}(\mathbf{x}_i)\| \geq \frac{\sigma C_m}{C_M} \|\mathbf{x}_{i+1} - \mathbf{x}_i\|, \quad (52)$$

where the last inequality is valid because

$$\|\mathbf{x}_{k+1} - \mathbf{x}_k\| = \alpha_k \|\mathbf{p}_k\| \leq \alpha_k C_M \|\mathbf{g}(\mathbf{x}_k)\|. \quad (53)$$

The upper bound of $\|\mathbf{x}_{k+1} - \mathbf{x}_*\|$ is

$$\begin{aligned}
\|\mathbf{x}_{k+1} - \mathbf{x}_*\| &\leq \sum_{i=1}^k \|\mathbf{x}_{i+1} - \mathbf{x}_i\| + \|\mathbf{x}_1 - \mathbf{x}_*\| \\
&\leq \frac{C_M}{\sigma C_m} \sum_{i=1}^k \phi(f(\mathbf{x}_i)) - \phi(f(\mathbf{x}_{i+1})) + \|\mathbf{x}_1 - \mathbf{x}_*\| \\
&\leq \frac{C_M}{\sigma C_m} (\phi(f(\mathbf{x}_1)) - \phi(f(\mathbf{x}_{k+1}))) + \|\mathbf{x}_1 - \mathbf{x}_*\| \\
&\leq \frac{C_M}{\sigma C_m} \phi(f(\mathbf{x}_1)) + \|\mathbf{x}_1 - \mathbf{x}_*\| \\
&< \delta,
\end{aligned} \tag{54}$$

which means $\mathbf{x}_{k+1} \in \mathcal{A}(\mathbf{x}_*, \delta)$ and (46) holds. Moreover, according to (52), we obtain

$$\sum_{k=1}^{\infty} \|\mathbf{x}_{k+1} - \mathbf{x}_k\| \leq \frac{C_M}{\sigma C_m} \sum_{k=1}^{\infty} \phi(f(\mathbf{x}_k)) - \phi(f(\mathbf{x}_{k+1})) \leq \frac{C_M}{\sigma C_m} \phi(f(\mathbf{x}_1)). \tag{55}$$

Thus, the proof of (47) is complete. \square

The sequence of iterates $\{\mathbf{x}_k\}$ is demonstrated to converge to a unique accumulation point next.

Theorem 5.8. *Suppose that Algorithm 2 generates an infinite sequence of iterates $\{\mathbf{x}_k\}$. $\{\mathbf{x}_k\}$ converges to a unique first-order stationary point \mathbf{x}_* , i.e.*

$$\lim_{k \rightarrow \infty} \mathbf{x}_k = \mathbf{x}_*. \tag{56}$$

Proof. Clearly, according to (55), the sequence $\{\mathbf{x}_k\}$ satisfies

$$\sum_{k=1}^{\infty} \|\mathbf{x}_{k+1} - \mathbf{x}_k\| < +\infty \tag{57}$$

and is a Cauchy sequence. Owing to the boundedness of $\{\mathbf{x}_k\}$, there exists an accumulate point \mathbf{x}_* of iterates $\{\mathbf{x}_k\}$. Thus (56) holds. \square

6. Numerical experiments. In this section we demonstrate the performance of our proposed TTDSR method on two datasets. The method is implemented with parameters $l = 5$, $\sigma = 0.01$, $\beta = 0.5$, $\mu = 1$. The stopping criteria is

$$\|\mathbf{g}(\mathbf{x}_k)\|_{\infty} < 10^{-10}$$

or

$$\|\mathbf{x}_{k+1} - \mathbf{x}_k\|_{\infty} < 10^{-16} \quad \text{and} \quad |f(\mathbf{x}_{k+1}) - f(\mathbf{x}_k)| < 10^{-2}.$$

The maximum number of iteration is set to 400. All simulations are run on a HP notebook with 2.5 GHz Intel Core i5 and 4 GB RAM. We use tensorlab 3.0 [26] for basic tensor operations.

In the numerical experiments, the groundtruth image SRI is artificially degraded to HSI and MSI based on P_1 , P_2 and P_3 . For matrices P_1 and P_2 of spatial degradation, we follow the Wald's protocol [36] and the degradation process from SRI to HSI is a combination of spatial blurring Gaussian kernel and downsampling. The downsampling and Gaussian kernel have parameters d and q , respectively. It is common to set the downsampling ratio $d = 4$ and $q = 9$ in the Gaussian kernel.

Image name	SRI	HSI	MSI
Indian pines, d=4	$144 \times 144 \times 200$	$36 \times 36 \times 200$	$144 \times 144 \times 6$
Indian pines, d=6	$144 \times 144 \times 200$	$24 \times 24 \times 200$	$144 \times 144 \times 6$
Salinas-A scene	$80 \times 80 \times 200$	$20 \times 20 \times 200$	$80 \times 80 \times 4$

TABLE 1. Image size for the SRI experiments.

In the following experiments, we also conduct simulations under situations such as $d = 6$ and $q = 9$, $d = 4$ and $q = 5$ respectively. In order to obtain MSI from SRI, we generate the spectral degradation matrix P_3 through spectral specifications, which are taken from LANDSAT or QuickBird specifications of multispectral sensors. The Indian pines and Salinas-A scene datasets are available online at [14]. For Indian pines, the groundtruth image SRI is degraded with the former sensor, while the SRI of Salinas-A scene is degraded with the latter as in [28]. The dimensions of HSI, MSI, SRI images are demonstrated in Table 1.

6.1. Comparison with other algorithms. In this subsection we compare the proposed algorithm with state-of-the-art approaches, including HySure [31] and FUSE [35], which are based on matrix decompositions. Furthermore, tensor CP [20] and tucker decomposition [28] methods are also considered. The HySure method is about a convex formulation for SRI via subspace-based regularization proposed by Simoés et al, while FUSE describes fast fusion of multiband images based on solving a Sylvester equation proposed by Wei et al. We calculate the following metrics to evaluate the effect of image fusion, which includes re-constructed signal-to-noise ratio (R-SNR), correlation coefficient (CC), spectral angle mapper (SAM) and the relative dimensional global error (ERGAS) used in [28]. R-SNR and CC are given by

$$\text{R-SNR} = 10 \log_{10} \left(\frac{\|\mathcal{Z}\|_F^2}{\|\hat{\mathcal{Z}} - \mathcal{Z}\|_F^2} \right) \quad (58)$$

and

$$\text{CC} = \frac{1}{n_3} \left(\sum_{k=1}^{n_3} \rho(\mathcal{Z}_{:, :, k}, \hat{\mathcal{Z}}_{:, :, k}) \right), \quad (59)$$

where $\rho(\cdot, \cdot)$ is the pearson correlation coefficient between the original and estimated spectral slices. The metric SAM is

$$\text{SAM} = \frac{1}{m_1 m_2} \sum_{n=1}^{m_1 m_2} \arccos \left(\frac{\mathcal{Z}_{n,:}^{(3)\top} \hat{\mathcal{Z}}_{n,:}^{(3)}}{\|\mathcal{Z}_{n,:}^{(3)}\|_2 \|\hat{\mathcal{Z}}_{n,:}^{(3)}\|_2} \right) \quad (60)$$

and calculates the angle between the original and estimated spectral fiber. The performance measurement ERGAS is

$$\text{ERGAS} = \frac{100}{d} \sqrt{\frac{1}{m_1 m_2 n_3} \sum_{k=1}^{n_3} \frac{\|\hat{\mathcal{Z}}_{:, :, k} - \mathcal{Z}_{:, :, k}\|_F^2}{\mu_k^2}}, \quad (61)$$

where μ_k^2 is the mean value of $\hat{\mathcal{Z}}_{:, :, k}$. It represents the relative dimensionless global error between SRI and the estimated one. It is the root mean-square error averaged by the size of the SRI.

	Algorithm	quality evaluation metrics				
		R-SNR	CC	SAM	ERGAS	TIME(s)
	best value	$+\infty$	1	0	0	-
d=4 q=9	STERTO	24.8691	0.8335	2.8220	1.2812	2.3025
	SCOTT	16.4046	0.7617	7.2446	2.3651	0.5865
	HySure	18.9055	0.6971	5.7052	2.3045	39.9998
	FUSE	10.3359	0.6126	13.8561	4.5692	0.3635
	TTDSR	17.0350	0.6712	6.7452	3.1165	2.3624
d=6 q=9	STERTO	23.7512	0.7874	3.2923	0.9875	2.1344
	SCOTT	17.1569	0.7414	6.7436	1.5801	0.8730
	HySure	17.8228	0.6879	6.4205	1.6793	38.6143
	FUSE	11.9157	0.6134	11.8385	2.8082	0.3006
	TTDSR	17.0350	0.6712	6.7452	2.0777	2.1966
d=4 q=5	STERTO	24.8723	0.8338	2.8213	1.2791	1.7986
	SCOTT	15.5634	0.7218	7.6436	2.9810	0.5197
	HySure	16.8333	0.6729	6.9514	2.8192	37.9540
	FUSE	9.5533	0.5678	14.6419	5.8727	0.3169
	TTDSR	17.0350	0.6712	6.7452	3.1165	2.386

TABLE 2. Comparison of performance of different algorithms on Indian pines.

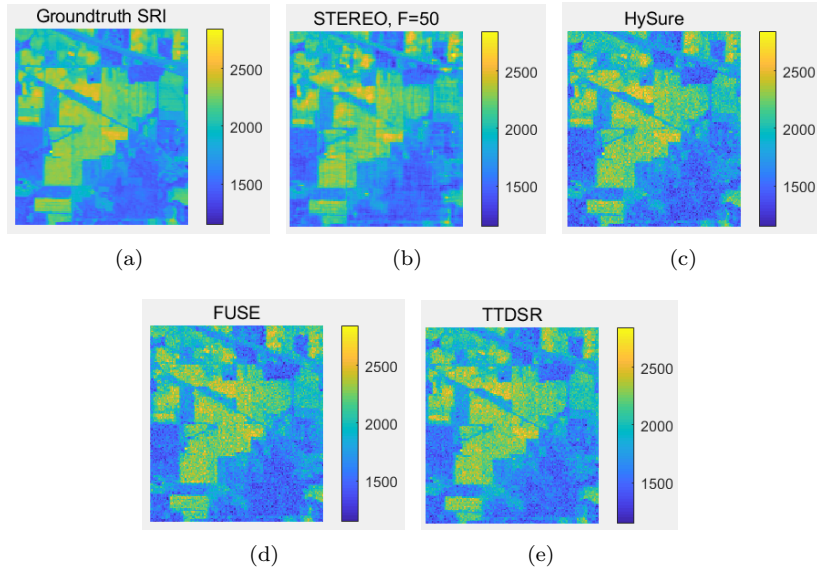


FIGURE 3. Spectral slice 120 of the SRI, Indian pines.

In practical applications, it is common that the hyperspectral and multispectral images generated by special sensors are noisy. Therefore in the experiments, we add white Gaussian noise to HSI and MSI. The first experiment is performed using Indian pines dataset from hyperspectral remote sensing data platform [14]. White Gaussian noise to \mathcal{Y}_h is 21dB, while to \mathcal{Y}_m is 25dB. The results are presented in Table

	Algorithm	quality evaluation metrics				
		R-SNR	CC	SAM	ERGAS	TIME(s)
	best value	$+\infty$	1	0	0	-
d=4	STERTO	17.1952	0.987	0.4548	4.3075	1.1343
	SCOTT	18.8878	0.9903	0.3651	3.8203	0.1726
	HySure	18.3815	0.9890	0.3519	4.0037	9.0540
q=9	FUSE	9.5258	0.8919	0.3769	12.2427	0.1248
	TTDSR	17.1458	0.9858	0.1089	4.5147	1.5402

TABLE 3. Comparison of performance of different algorithms on Salinas-A scene.

2 and Figure 3. The rank of tucker decomposition in SCOTT is $[70, 70, 6]$. According to [20], tensor rank $F = 50$ of the STEREO method often yields good performance. For HySure method, ‘E’ represents groundtruth number of materials and is set to 16, which is chosen as the number of endmembers as [20]. In Table 2, when $d = 4$ and $q = 9$, the STERTO method performs the best and our proposed algorithm has advantages over the FUSE method in terms of metrics R-SNR, CC, SAM, and ERGAS. The HySure method has comparable performance to our algorithm, but requires more computational time. Moreover, our proposed algorithm gets a higher R-SNR value and lower SAM value when compared to the SCOTT. Figure 3 also provides an intuitive and reasonable display of super-resolution images.

In addition, we demonstrate the results given by different algorithms for Indian pines in Table 2 under the conditions $d = 6, q = 9$, and $d = 4, q = 5$. It seems that the values d and q affect the performances of all methods in some degree. However, the ranking of each evaluation parameters of different methods almost do not change when d and q vary.

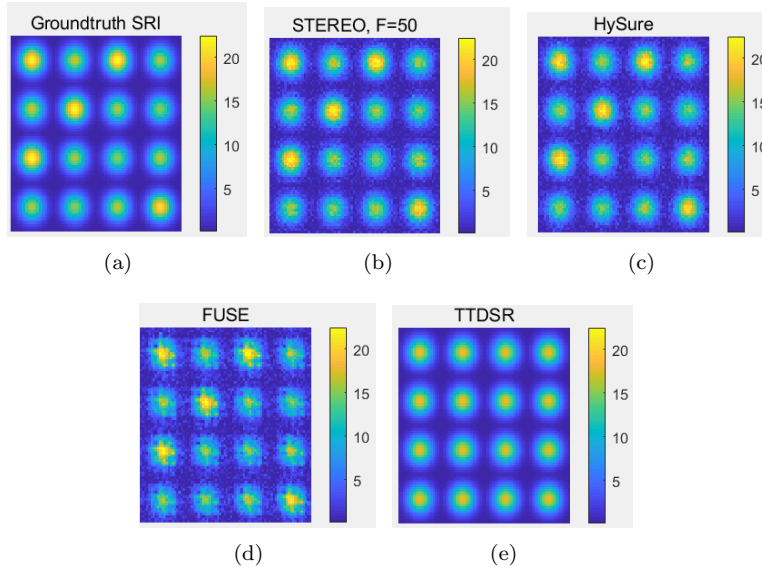


FIGURE 4. Spectral slice 120 of the SRI, Salinas-A scene.

In the second example, Salinas-A scene dataset comes from the hyperspectral remote sensing data platform, which is available in [28]. Similarly, white Gaussian noise is added to \mathcal{Y}_h and \mathcal{Y}_m with an input SNR of 30 dB. Consistently, we conduct experiments on the dataset under the conditions of $d = 4, q = 9$, and the results are shown in Table 3. It is found that when $d = 6, q = 9$ or $d = 4, q = 5$ the metrics of the listed algorithms are almost consistent with the results of $d = 4, q = 9$. We omit results of under these two conditions. In Table 3, compared with the STERTO, our proposed algorithm has comparable signal-to-noise ratio and time. Compared to other algorithms, our method get the lowest SAM value. Furthermore, it is evident that the TTDSR algorithm performs better than FUSE. In Figure 4, the super-resolution images obtained by different algorithms are shown. Due to the low SAM value, the image recovered by TTDSR algorithm are relatively clearer.

6.2. Further numerical results of TTDSR. In this subsection we further show the numerical results of TTDSR implemented on Indian pines dataset. The curve in Figure 5(a) displays the objective function value in each iteration, which verifies the theoretical conclusion that the sequence $\{f(\mathbf{x}_k)\}$ is decreasing.

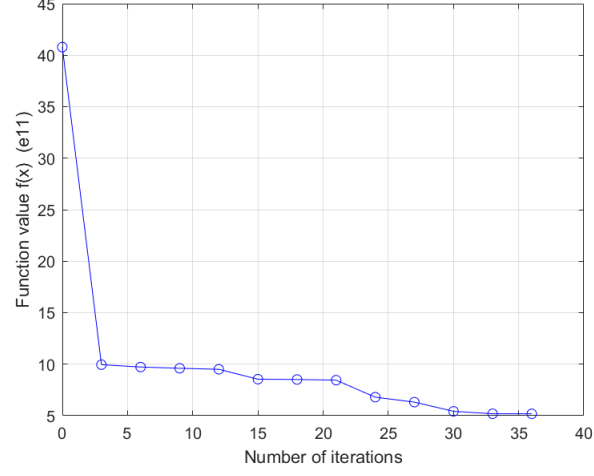
In theory, the SRI is a low rank tensor. However, in the numerical experiments, we have no prior knowledge of the triple rank of the SRI tensor and the rank is given artificially. For Indian pines dataset, we run TTDSR algorithm ten times with the triple rank changing from 1 to 10 accordingly. In Figure 5(b), we demonstrate the values of R-SNR corresponding to different triple ranks. In this example, the best R-SNR is attained when the triple rank is 1.

From the above analysis, we can see that among all algorithms, the HySure method performs the best but costs much more time than others. This is because it establishes an optimization problem of convex objective function with vector total variation regularization. The TV regularizer calculates the dispersion difference of the image in the horizontal and vertical directions. Our method has a significant advantage over the SCOTT in that we only need to consider a triple rank, while the rank of tucker decomposition [28] is an array.

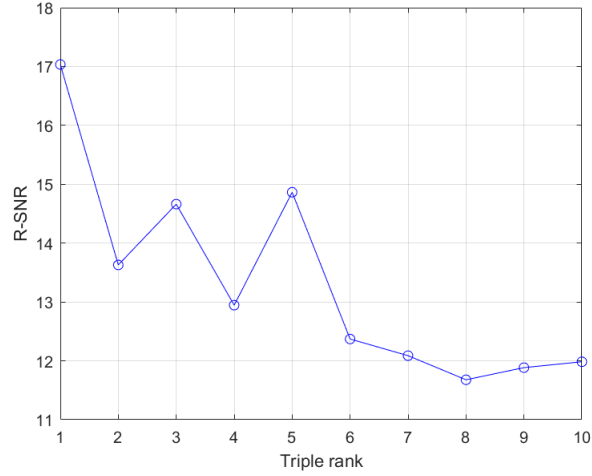
7. Conclusion. In this work, we provide a novel tensor triple decomposition model for hyperspectral super-resolution. Firstly, in order to capture the global interdependence between hyperspectral data of different modes, we use triple rank to characterize its low rank. Then we propose a optimization algorithm TTDSR to get the desired hyperspectral super-resolution image. Using the triple decomposition theorem, we cleverly obtain the gradient of the objective function of the model, which provides great help for solving the problem. Due to the algebraic nature of the objective function $f(\mathbf{x})$, we apply the Kurdyka-Lojasiewicz property in analyzing the convergence of the sequence of iterates generated by TTDSR. In addition, experiments on two datasets show the feasibility and effectiveness of the TTDSR. This work opens up a new prospect for realizing hyperspectral super-resolution by using various tensor decompositions.

Appendix A. The process of vectorization of the variable. The gradient of the objective function in (12) is calculated by vectorization of the variable as

$$\mathbf{x} := \begin{pmatrix} \mathbf{a}_{m_1 r r} \\ \mathbf{b}_{m_2 r r} \\ \mathbf{c}_{n_3 r r} \end{pmatrix} = \begin{pmatrix} A_{m_1 r r \times 1} \\ B_{m_2 r r \times 1} \\ C_{n_3 r r \times 1} \end{pmatrix}. \quad (62)$$



(a)



(b)

FIGURE 5. Further experiments on Indian pines.

We directly vectorize the optimal variables of (12) in accordance with preset principles while dealing with small-scale data. Firstly, noting that $f(\mathbf{x}) = f_1(\mathbf{x}) + f_2(\mathbf{x}) + f_3(\mathbf{x})$. Secondly, vectorizing the known tensors $\mathcal{Y}_h, \mathcal{Y}_m$, we get

$$\text{vec}(\mathcal{Y}_h) = \mathbf{d}_h \quad \text{and} \quad \text{vec}(\mathcal{Y}_m) = \mathbf{d}_m.$$

The symbol vec indicates the vectorization operator. It yields from (21) that

$$\begin{aligned} (\mathbf{y}_h)_{n_1 n_2 n_3} &= \left(\left((C_{lm \times n_3} \otimes E_{n_2})^\top \otimes P_{n_1 \times m_1} \right) \left((E_m \otimes K_{n \times n_2 l})^\top \otimes E_{m_1} \right) \right) \mathbf{a}_{m_1 n m} \\ &= (C_{n_3 \times l m} \otimes E_{n_2} \otimes P_{n_1 \times m_1}) (E_m \otimes K_{n_2 l \times n} \otimes E_{m_1}) \mathbf{a}_{m_1 n m} \\ &= (C_{n_3 \times l m} \otimes P_{n_1 n_2 \times m_1 n_2}) (E_m \otimes K_{n_2 l \times n} \otimes E_{m_1}) \mathbf{a}_{m_1 n m}. \end{aligned}$$

Hence,

$$f_1(\mathbf{x}) = \|(C_{n_3 \times lm} \otimes P_{n_1 n_2 \times m_1 n_2})(E_m \otimes K_{n_2 l \times n} \otimes E_{m_1}) \mathbf{a}_{m_1 n m} - \mathbf{d}_h\|_2^2.$$

It is easy to see

$$\begin{aligned} \frac{\partial f_1(\mathbf{x})}{\partial \mathbf{a}_{m_1 n m}} &= 2((C_{n_3 \times lm} \otimes P_{n_1 n_2 \times m_1 n_2})(E_m \otimes K_{n_2 l \times n} \otimes E_{m_1}))^\top \\ &\quad \cdot ((C_{n_3 \times lm} \otimes P_{n_1 n_2 \times m_1 n_2})(E_m \otimes K_{n_2 l \times n} \otimes E_{m_1}) \mathbf{a}_{m_1 n m} - \mathbf{d}_h) \\ &= 2(E_m \otimes K_{n \times n_2 l} \otimes E_{m_1})(C_{lm \times n_3} \otimes P_{m_1 n_2 \times n_1 n_2}) \\ &\quad \cdot ((C_{n_3 \times lm} \otimes P_{n_1 n_2 \times m_1 n_2})(E_m \otimes K_{n_2 l \times n} \otimes E_{m_1}) \mathbf{a}_{m_1 n m} - \mathbf{d}_h). \end{aligned}$$

Similarly, it yields from (24) that

$$\begin{aligned} (\mathbf{y}_m)_{m_1 m_2 m_3} &= \left((E_m \otimes B_{n \times m_2 l})(G_{lm \times m_3} \otimes E_{m_2})^\top \otimes E_{m_1} \right) \mathbf{a}_{m_1 n m} \\ &= ((G_{m_3 \times lm} \otimes E_{m_1 m_2})(E_m \otimes B_{m_2 l \times n} \otimes E_{m_1})) \mathbf{a}_{m_1 n m}. \end{aligned}$$

Hence,

$$f_2(\mathbf{x}) = \|((G_{m_3 \times lm} \otimes E_{m_1 m_2})(E_m \otimes B_{m_2 l \times n} \otimes E_{m_1})) \mathbf{a}_{m_1 n m} - \mathbf{d}_m\|_2^2,$$

and

$$\begin{aligned} \frac{\partial f_2(\mathbf{x})}{\partial \mathbf{a}_{m_1 n m}} &= 2((G_{m_3 \times lm} \otimes E_{m_1 m_2})(E_m \otimes B_{m_2 l \times n} \otimes E_{m_1}))^\top \\ &\quad \cdot ((G_{m_3 \times lm} \otimes E_{m_1 m_2})(E_m \otimes B_{m_2 l \times n} \otimes E_{m_1}) \mathbf{a}_{m_1 n m} - \mathbf{d}_m) \\ &= 2(E_m \otimes B_{n \times m_2 l} \otimes E_{m_1})(G_{lm \times m_3} \otimes E_{m_1 m_2}) \\ &\quad \cdot ((G_{m_3 \times lm} \otimes E_{m_1 m_2})(E_m \otimes B_{m_2 l \times n} \otimes E_{m_1}) \mathbf{a}_{m_1 n m} - \mathbf{d}_m). \end{aligned}$$

For $f_3(\mathbf{x}) = \mu \|\mathbf{x}\|_2^2$, we have

$$\frac{\partial f_3(\mathbf{x})}{\partial \mathbf{a}_{m_1 n m}} = 2\mu \mathbf{a}_{m_1 n m}.$$

In a word,

$$\begin{aligned} \frac{\partial f(\mathbf{x})}{\partial \mathbf{a}_{m_1 n m}} &= 2(E_m \otimes K_{n \times n_2 l} \otimes E_{m_1})(C_{lm \times n_3} \otimes P_{m_1 n_2 \times n_1 n_2}) \\ &\quad \cdot (((C_{n_3 \times lm} \otimes P_{n_1 n_2 \times m_1 n_2})(E_m \otimes K_{n_2 l \times n} \otimes E_{m_1})) \mathbf{a}_{m_1 n m} - \mathbf{d}_h) \\ &\quad + 2(E_m \otimes B_{n \times m_2 l} \otimes E_{m_1})(G_{lm \times m_3} \otimes E_{m_1 m_2}) \\ &\quad \cdot (((G_{m_3 \times lm} \otimes E_{m_1 m_2})(E_m \otimes B_{m_2 l \times n} \otimes E_{m_1})) \mathbf{a}_{m_1 n m} - \mathbf{d}_m) \\ &\quad + 2\mu \mathbf{a}_{m_1 n m}. \end{aligned} \tag{63}$$

It yields from (22) and (25) that

$$f_1(\mathbf{x}) = \|((H_{n_1 \times mn} \otimes P_{n_2 n_3 \times m_2 n_3})(E_n \otimes C_{n_3 m \times l} \otimes E_{m_2})) \mathbf{b}_{m_2 l n} - \mathbf{d}_h\|_2^2,$$

$$f_2(\mathbf{x}) = \|((A_{m_1 \times mn} \otimes E_{m_2 m_3})(E_n \otimes G_{m_3 m \times l} \otimes E_{m_2})) \mathbf{b}_{m_2 l n} - \mathbf{d}_m\|_2^2,$$

and

$$f_3(\mathbf{x}) = \mu \|\mathbf{x}\|_2^2.$$

Therefore,

$$\begin{aligned}
\frac{\partial f(\mathbf{x})}{\partial \mathbf{b}_{m_2 l n}} &= 2(E_n \otimes C_{l \times n_3 m} \otimes E_{m_2})(H_{m n \times n_1} \otimes P_{m_2 n_3 \times n_2 n_3}) \\
&\quad \cdot (((H_{n_1 \times m n} \otimes P_{n_2 n_3 \times m_2 n_3})(E_n \otimes C_{n_3 m \times l} \otimes E_{m_2})) \mathbf{b}_{m_2 l n} - \mathbf{d}_h) \\
&\quad + 2(E_n \otimes G_{l \times m_3 m} \otimes E_{m_2})(A_{m n \times m_1} \otimes E_{m_2 m_3}) \\
&\quad \cdot (((A_{m_1 \times m n} \otimes E_{m_2 m_3})(E_n \otimes G_{m_3 m \times l} \otimes E_{m_2})) \mathbf{b}_{m_2 l n} - \mathbf{d}_m) \\
&\quad + 2\mu \mathbf{b}_{m_2 l n}.
\end{aligned} \tag{64}$$

It also yields from (23) and (26) that

$$f_1(\mathbf{x}) = \|((H_{n_1 \times n m} \otimes E_{n_2 n_3})(E_m \otimes K_{n_2 n \times l} \otimes E_{n_3})) \mathbf{c}_{n_3 l m} - \mathbf{d}_h\|_2^2,$$

$$f_2(\mathbf{x}) = \|((A_{m_1 \times n m} \otimes P_{m_2 m_3 \times m_2 n_3})(E_m \otimes B_{m_2 n \times l} \otimes E_{n_3})) \mathbf{c}_{n_3 l m} - \mathbf{d}_m\|_2^2,$$

and

$$f_3(\mathbf{x}) = \mu \|\mathbf{x}\|_2^2.$$

Thus,

$$\begin{aligned}
\frac{\partial f(\mathbf{x})}{\partial \mathbf{c}_{n_3 l m}} &= 2(E_m \otimes K_{l \times n_2 n} \otimes E_{n_3})(H_{n m \times n_1} \otimes E_{n_2 \times n_3}) \\
&\quad \cdot (((H_{n_1 \times n m} \otimes E_{n_2 \times n_3})(E_m \otimes K_{n_2 n \times l} \otimes E_{n_3})) \mathbf{c}_{n_3 l m} - \mathbf{d}_h) \\
&\quad + 2(E_m \otimes B_{l \times m_2 n} \otimes E_{n_3})(A_{n m \times m_1} \otimes P_{m_2 n_3 \times m_2 m_3}) \\
&\quad \cdot (((A_{m_1 \times n m} \otimes P_{m_2 m_3 \times m_2 n_3})(E_m \otimes B_{m_2 n \times l} \otimes E_{n_3})) \mathbf{c}_{n_3 l m} - \mathbf{d}_m) \\
&\quad + 2\mu \mathbf{c}_{n_3 l m}.
\end{aligned} \tag{65}$$

Then, its gradient is

$$\begin{aligned}
\nabla f(\mathbf{x}) &= 2 \left(\begin{aligned}
&(E_m \otimes K_{n \times n_2 l} \otimes E_{m_1})(C_{l m \times n_3} \otimes P_{m_1 n_2 \times n_1 n_2}) \\
&\quad \cdot (((C_{n_3 \times l m} \otimes P_{n_1 n_2 \times m_1 n_2})(E_m \otimes K_{n_2 l \times n} \otimes E_{m_1})) \mathbf{a}_{m_1 n m} - \mathbf{d}_h) \\
&\quad + 2(E_m \otimes B_{n \times m_2 l} \otimes E_{m_1})(G_{l m \times m_3} \otimes E_{m_1 m_2}) \\
&\quad \cdot (((G_{m_3 \times l m} \otimes E_{m_1 m_2})(E_m \otimes B_{m_2 l \times n} \otimes E_{m_1})) \mathbf{a}_{m_1 n m} - \mathbf{d}_m) \\
&\quad + 2\mu \mathbf{a}_{m_1 n m} \\
&\quad \hline
&(E_n \otimes C_{l \times n_3 m} \otimes E_{m_2})(H_{m n \times n_1} \otimes P_{m_2 n_3 \times n_2 n_3}) \\
&\quad \cdot (((H_{n_1 \times m n} \otimes P_{n_2 n_3 \times m_2 n_3})(E_n \otimes C_{n_3 m \times l} \otimes E_{m_2})) \mathbf{b}_{m_2 l n} - \mathbf{d}_h) \\
&\quad + 2(E_n \otimes G_{l \times m_3 m} \otimes E_{m_2})(A_{m n \times m_1} \otimes E_{m_2 m_3}) \\
&\quad \cdot (((A_{m_1 \times m n} \otimes E_{m_2 m_3})(E_n \otimes G_{m_3 m \times l} \otimes E_{m_2})) \mathbf{b}_{m_2 l n} - \mathbf{d}_m) \\
&\quad + 2\mu \mathbf{b}_{m_2 l n} \\
&\quad \hline
&(E_m \otimes K_{l \times n_2 n} \otimes E_{n_3})(H_{n m \times n_1} \otimes E_{n_2 \times n_3}) \\
&\quad \cdot (((H_{n_1 \times n m} \otimes E_{n_2 \times n_3})(E_m \otimes K_{n_2 n \times l} \otimes E_{n_3})) \mathbf{c}_{n_3 l m} - \mathbf{d}_h) \\
&\quad + 2(E_m \otimes B_{l \times m_2 n} \otimes E_{n_3})(A_{n m \times m_1} \otimes P_{m_2 n_3 \times m_2 m_3}) \\
&\quad \cdot (((A_{m_1 \times n m} \otimes P_{m_2 m_3 \times m_2 n_3})(E_m \otimes B_{m_2 n \times l} \otimes E_{n_3})) \mathbf{c}_{n_3 l m} - \mathbf{d}_m) \\
&\quad + 2\mu \mathbf{c}_{n_3 l m}
\end{aligned} \right). \tag{66}
\end{aligned}$$

Appendix B. We introduce five lemmas for the proof of Lemma 5.2. First, we consider the BFGS update (14), (15), (16).

Lemma B.1. *Suppose that H_{k+1} is generated by (16). Then, we have*

$$\|H_{k+1}\| \leq \|H_k\| \left(1 + \frac{2MN}{\epsilon}\right)^2 + \frac{N^2}{\epsilon}. \quad (67)$$

Proof. If $\mathbf{y}_k^\top \mathbf{s}_k < \epsilon$, we get $\rho_k = 0$ and $H_{k+1} = H_k$. Hence, the inequality (67) holds. Next, we consider the case $\mathbf{y}_k^\top \mathbf{s}_k \geq \epsilon$. Obviously, $\rho_k \leq \frac{1}{\epsilon}$. From Lemma 5.1 and $\{\mathbf{x}_k\}$ is bounded, suppose there exists a positive number N such that $\|\mathbf{s}_k\| \leq N$ and we get

$$\|\mathbf{y}_k\| \leq 2M. \quad (68)$$

Since

$$\|V_k\| \leq 1 + \rho_k \|\mathbf{y}_k\| \|\mathbf{s}_k\| \leq 1 + \frac{2MN}{\epsilon} \quad \text{and} \quad \|\rho_k \mathbf{s}_k \mathbf{s}_k^\top\| \leq \rho_k \|\mathbf{s}_k\|^2 \leq \frac{N^2}{\epsilon}, \quad (69)$$

we have

$$\|H_{k+1}\| \leq \|H_k\| \|V_k\|^2 + \|\rho_k \mathbf{s}_k \mathbf{s}_k^\top\| \leq \|H_k\| \left(1 + \frac{2MN}{\epsilon}\right)^2 + \frac{N^2}{\epsilon}. \quad (70)$$

Hence, the inequality (67) is valid. \square

Lemma B.2. *Suppose that H_k is positive definite and H_{k+1} is generated by BFGS (14), (15), (16). Let $\lambda_{\min}(H)$ be the smallest eigenvalue of a symmetric matrix H . Then, we get H_{k+1} is positive definite and*

$$\lambda_{\min}(H_{k+1}) \geq \frac{\epsilon}{\epsilon + 4M^2 \|H_k\|} \lambda_{\min}(H_k). \quad (71)$$

Proof. For any unit vector \mathbf{v} , we have

$$\mathbf{v}^\top H_{k+1} \mathbf{v} = (\mathbf{v} - \rho_k \mathbf{s}_k^\top \mathbf{v} \mathbf{y}_k)^\top H_k (\mathbf{v} - \rho_k \mathbf{s}_k^\top \mathbf{v} \mathbf{y}_k) + \rho_k (\mathbf{s}_k^\top \mathbf{v})^2. \quad (72)$$

Let $t \equiv \mathbf{s}_k^\top \mathbf{v}$ and

$$\phi(t) \equiv (\mathbf{v} - t \rho_k \mathbf{y}_k)^\top H_k (\mathbf{v} - t \rho_k \mathbf{y}_k) + \rho_k t^2. \quad (73)$$

Because H_k is positive definite, $\phi(t)$ is convex and attaches its minimum at $t_* = \frac{\rho_k \mathbf{y}_k^\top H_k \mathbf{v}}{\rho_k + \rho_k^2 \mathbf{y}_k^\top H_k \mathbf{y}_k}$. Hence,

$$\begin{aligned} \mathbf{v}^\top H_{k+1} \mathbf{v} &\geq \phi(t_*) \\ &= \mathbf{v}^\top H_k \mathbf{v} - t_* \rho_k \mathbf{y}_k^\top H_k \mathbf{v} \\ &= \frac{\rho_k \mathbf{v}^\top H_k \mathbf{v} + \rho_k^2 \left(\mathbf{y}_k^\top H_k \mathbf{y}_k \mathbf{v}^\top H_k \mathbf{v} - (\mathbf{y}_k^\top H_k \mathbf{v})^2 \right)}{\rho_k + \rho_k^2 \mathbf{y}_k^\top H_k \mathbf{y}_k} \\ &\geq \frac{\mathbf{v}^\top H_k \mathbf{v}}{1 + \rho_k \mathbf{y}_k^\top H_k \mathbf{y}_k} > 0, \end{aligned} \quad (74)$$

where the penultimate inequality holds because the Cauchy-Schwarz inequality is valid for the positive definite matrix norm $\|\cdot\|_{H_k}$,

$$\|\mathbf{y}_k\|_{H_k} \|\mathbf{v}\|_{H_k} \geq \mathbf{y}_k^\top H_k \mathbf{v}. \quad (75)$$

So H_{k+1} is also positive definite. From (68), it is easy to verify that

$$1 + \rho_k \mathbf{y}_k^\top H_k \mathbf{y}_k \leq 1 + \frac{4M^2 \|H_k\|}{\epsilon}. \quad (76)$$

Thus, we have

$$\mathbf{v}^\top H_{k+1} \mathbf{v} \geq \frac{\epsilon}{\epsilon + 4M^2 \|H_k\|} \lambda_{\min}(H_k). \quad (77)$$

Hence, we get the validation of (71). \square

Second, we turn to L-BFGS. Regardless of the selection of γ_k in (19), we get the following lemma.

Lemma B.3. *Suppose that the parameter γ_k takes Barzilai-Borwein steps (19). Then, we have*

$$\frac{\epsilon}{4M^2} \leq \gamma_k \leq \frac{N^2}{\epsilon}. \quad (78)$$

Proof. If $\mathbf{y}_k^\top \mathbf{s}_k < \epsilon$, we get $\gamma_k = 1$ which satisfies the bounds in (78) obviously. Otherwise, we have

$$\epsilon \leq \mathbf{y}_k^\top \mathbf{s}_k \leq \|\mathbf{y}_k\| \|\mathbf{s}_k\|. \quad (79)$$

Recalling (68), we get

$$\frac{\epsilon}{N} \leq \|\mathbf{y}_k\| \leq 2M \quad \text{and} \quad \frac{\epsilon}{2M} \leq \|\mathbf{s}_k\| \leq N. \quad (80)$$

Hence, we have

$$\frac{\epsilon}{4M^2} \leq \frac{\mathbf{y}_k^\top \mathbf{s}_k}{\|\mathbf{y}_k\|^2} \leq \frac{\|\mathbf{y}_k\| \|\mathbf{s}_k\|}{\|\mathbf{y}_k\|^2} = \frac{\|\mathbf{s}_k\|}{\|\mathbf{y}_k\|} = \frac{\|\mathbf{s}_k\|^2}{\|\mathbf{y}_k\| \|\mathbf{s}_k\|} \leq \frac{\|\mathbf{s}_k\|^2}{\mathbf{y}_k^\top \mathbf{s}_k} \leq \frac{N^2}{\epsilon}. \quad (81)$$

which means that γ_k^{BB1} and γ_k^{BB2} satisfy (78). \square

Third, based on Lemmas B.1, B.2, B.3, we obtain two lemmas as follows.

Lemma B.4. *Suppose that the approximation of a Hessian's inverse H_k is generated by L-BFGS (17), (18). Then, there exists a positive constant $C_M \geq 1$ such that*

$$\|H_k\| \leq C_M. \quad (82)$$

Proof. From Lemma B.3 and (18), we have $\|H_k^{(0)}\| \leq \frac{N^2}{\epsilon}$. Then, for (17) and Lemma B.1, we get

$$\begin{aligned} \|H_k\| &\leq \|H_{k-1}\| \left(1 + \frac{2MN}{\epsilon}\right)^2 + \frac{N^2}{\epsilon} \\ &\leq \dots \\ &\leq \|H_k^{(0)}\| \left(1 + \frac{2MN}{\epsilon}\right)^{2l} + \frac{N^2}{\epsilon} \sum_{m=1}^{l-1} \left(1 + \frac{2MN}{\epsilon}\right)^{2m} \\ &\leq \frac{N^2}{\epsilon} \sum_{m=1}^l \left(1 + \frac{2MN}{\epsilon}\right)^{2m} \equiv C_M. \end{aligned} \quad (83)$$

Thus (82) holds. \square

Lemma B.5. *Suppose that the approximation of a Hessian's inverse H_k is generated by L-BFGS (17), (18). Then, there exists a constant $0 < C_m < 1$ such that*

$$\lambda_{\min}(H_k) \geq C_m. \quad (84)$$

Proof. From Lemma B.3 and (18), we have $\lambda_{\min}(H_k^{(0)}) \geq \frac{\epsilon}{4M^2}$. Moreover, Lemma B.4 means $\|H_{k-m}\| \leq C_M$ for all $m = 1, \dots, l$. Hence, Lemma B.2 implies

$$\lambda_{\min}(H_{k-m+1}) \geq \frac{\epsilon}{\epsilon + 4M^2C_M} \lambda_{\min}(H_{k-m}). \quad (85)$$

Then, we obtain

$$\begin{aligned} \lambda_{\min}(H_k) &\geq \frac{\epsilon}{\epsilon + 4M^2C_M} \lambda_{\min}(H_{k-1}) \\ &\geq \dots \\ &\geq \left(\frac{\epsilon}{\epsilon + 4M^2C_M} \right)^l \lambda_{\min}(H_k^{(0)}) \\ &\geq \frac{\epsilon}{4M^2} \left(\frac{\epsilon}{\epsilon + 4M^2C_M} \right)^l \equiv C_m. \end{aligned} \quad (86)$$

Finally, the proof of Lemma 5.2 is straightforward from Lemmas B.4 and B.5. \square

REFERENCES

- [1] B. Aiazzi, S. Baronti and M. Selva, [Improving component substitution pansharpening through multivariate regression of MS +Pan data](#), *IEEE Trans. Geosci. Remote Sens.*, **45** (2007), 3230-3239.
- [2] H. Attouch, J. Bolte, P. Redont and A. Soubeyran, [Proximal alternating minimization and projection methods for nonconvex problems: An approach based on the Kurdyka-Lojasiewicz inequality](#), *Math. Oper. Res.*, **35** (2010), 438-457.
- [3] J. Barzilai and J. M. Borwein, [Two-point step size gradient methods](#), *IMA. J. Numer. Anal.*, **8** (1988), 141-148.
- [4] J. M. Bioucas-Dias, A. Plaza, G. Camps-Valls, P. Scheunders, N. Nasrabadi and J. Chanussot, [Hyperspectral remote sensing data analysis and future challenges](#), *IEEE Geosci. Remote Sens. Mag.*, **1** (2013), 6-36.
- [5] R. A. Borsoi, C. Prévost, K. Usevich, D. Brie, J. C. Bermudez, and C. Richard, [Coupled tensor decomposition for hyperspectral and multispectral image fusion with inter-image variability](#), *IEEE J. Sel. Top. Signal Process.*, **15** (2021), 702-717.
- [6] P. Chavez, S. C. Sides and J. A. Anderson, Comparison of three different methods to merge multiresolution and multispectral data-Landsat TM and SPOT panchromatic, *Photogramm. Eng. Remote Sens.*, **57** (1991), 295-303.
- [7] C. I. Chang and S.S. Chiang, [Anomaly detection and classification for hyperspectral imagery](#), *IEEE Trans. Geosci. Remote Sens.*, **40** (2002), 1314-1325.
- [8] G. Camps-Valls and L. Bruzzone, [Kernel-based methods for hyperspectral image classification](#), *IEEE Trans. Geosci. Remote Sens.*, **43** (2005), 1351-1362.
- [9] Z. Chen, H. Pu, B. Wang and G. M. Jiang, [Fusion of hyperspectral and multispectral images: A novel framework based on generalization of pan-sharpening methods](#), *IEEE Geosci. Remote Sens. Lett.*, **11** (2014), 1418-1422.
- [10] J. Chang, Y. Chen, L. Qi, [Computing eigenvalues of large scale sparse tensors arising from a hypergraph](#), *SIAM J. Sci. Comput.*, **38** (2016), A3618-A3643.
- [11] Y. Chen, X. Zhang, L. Qi and Y. Xu, [A Barzilai Borwein gradient algorithm for spatio-temporal internet traffic data completion via tensor triple decomposition](#), *SIAM J. Sci. Comput.*, **88** (2021), 1-24.
- [12] E. J. Candès, X. Li, Y. Ma and J. Wright, [A robust principal component analysis](#), *Statistics: A Journal of Theoretical and Applied Statistics*, **58** (2011), 1-37.
- [13] R. Dian and S. Li, [Hyperspectral image super-resolution via subspace-based low tensor multi-rank regularization](#), *IEEE Trans. Image Process.*, **28** (2019), 5135-5146.
- [14] GIC, Grupo de inteligencia computacional, 2014. Available from: <http://www.ehu.es/ccwintco/index.php?title=HyperspectralRemoteSensingScenes>.
- [15] R. C. Hardie, M. T. Eismann and G. L. Wilson, [MAP estimation for hyperspectral image resolution enhancement using an auxiliary sensor](#), *IEEE Trans. Image Process.*, **13** (2004), 1174-1184.

- [16] W. He, Y. Chen, N. Yokoya, C. Li and Q. Zhao, [Hyperspectral super-resolution via coupled tensor ring factorization](#), *Pattern Recognit.*, **122** (2022), 108280.
- [17] T. Imbiriba, R. A. Borsoi, J. C. M. Bermudez, [Low-rank tensor modeling for hyperspectral unmixing accounting for spectral variability](#), *IEEE Trans. Geosci. Remote Sens.*, **58** (2019), 1833-1842.
- [18] N. Keshava, J. F. Mustard, [Spectral unmixing](#), *IEEE Signal Process. Mag.*, **19** (2002), 44-57.
- [19] R. Kawakami, Y. Matsushita, J. Wright, M. Ben-Ezra, Y. W. Tai, and K. Ikeuchi, [High-resolution hyperspectral imaging via matrix factorization](#), *Conference on Computer Vision and Pattern Recognition(CVPR)*, IEEE, (2011), 2329-2336.
- [20] C. I. Kanatsoulis, X. Fu, N. D. Sidiropoulos and W. K. Ma, [Hyperspectral super-resolution: A coupled tensor factorization approach](#), *IEEE Trans. Signal Process.*, **66** (2018), 6503-6517.
- [21] D. C. Liu and J. Nocedal, [On the limited memory BFGS method for large scale optimization](#), *Math. Program.*, **45** (1989), 503-528.
- [22] J. G. Liu, [Smoothing filter-based intensity modulation: A spectral preserve image fusion technique for improving spatial details](#), *Int. J. Remote Sens.*, **21** (2000), 3461-3472.
- [23] X. Liu, S. Bourennane, C. Fossati, [Denoising of hyperspectral images using the PARAFAC model and statistical performance analysis](#), *IEEE Trans. Geosci. Remote Sens.*, **50** (2012), 3717-3724.
- [24] S. Li, R. Dian, L. Fang and J. M. Bioucas-Dias, [Fusing hyperspectral and multispectral images via coupled sparse tensor factorization](#), *IEEE Trans. Image Process.*, **27** (2018), 4118-4130.
- [25] D. Manolakis and G. Shaw, [Detection algorithms for hyperspectral imaging applications](#), *IEEE Signal Process. Mag.*, **19** (2002), 29-43.
- [26] N. Vervliet, O. Debals, L. Sorber, M. Van Barel and L. De Lathauwer, Tensorlab 3.0, 2016. Available from: <http://www.tensorlab.net>.
- [27] X. Otazu, M. Gonzalez-Audcana and O. Fors, [Introduction of sensor spectral response into image fusion methods. Application to wavelet-based methods](#), *IEEE Trans. Geosci. Remote Sens.*, **43** (2005), 2376-2385.
- [28] C. Prévost, K. Usevich, P. Comon and D. Brie, [Hyperspectral super-resolution with coupled Tucker approximation: Recoverability and SVD-based algorithms](#), *IEEE Trans. Signal Process.*, **68** (2020), 931-946.
- [29] L. Qi, Y. Chen, M. Bakshi and X. Zhang, [Triple decomposition and tensor recovery of third order tensors](#), *SIAM J Matrix Anal Appl.*, **42** (2021), 299-329.
- [30] M. Selva, B. Aiazzi, F. Butera, L. Chiarantini and S. Baronti, [Hyper-sharpening: A first approach on SIM-GA data](#), *IEEE J. Sel. Top. Appl. Earth Observ. Remote Sens.*, **8** (2015), 3008-3024.
- [31] M. Simoes, J. Bioucas-Dias, L. B. Almeida and J. Chanussot, [A convex formulation for hyperspectral image superresolution via subspace-based regularization](#), *IEEE Trans. Geosci. Remote Sens.*, **53** (2014), 3373-3388.
- [32] G. Vivone, L. Alparone, J. Chanussot, M. Dalla Mura, A. Garzelli, G. A. Licciardi and L. Wald, [A critical comparison among pansharpening algorithms](#), *IEEE Trans. Geosci. Remote Sens.*, **53** (2014), 2565-2586.
- [33] M. A. Veganzones, J. E. Cohen, R. C. Farias, J. Chanussot and P. Comon, [Nonnegative tensor CP decomposition of hyperspectral data](#), *IEEE Trans. Geosci. Remote Sens.*, **54** (2015), 2577-2588.
- [34] Q. Wei, J. Bioucas-Dias, N. Dobigeon and J. Y. Tourneret, [Hyperspectral and multispectral image fusion based on a sparse representation](#), *IEEE Trans. Geosci. Remote Sens.*, **53** (2015), 3658-3668.
- [35] Q. Wei, N. Dobigeon and J. Y. Tourneret, [Fast fusion of multi-band images based on solving a Sylvester equation](#), *IEEE Trans. Image Process.*, **24** (2015), 4109-4121.
- [36] L. Wald, T. Ranchin and M. Mangolini, [Fusion of satellite images of different spatial resolutions: Assessing the quality of resulting images](#), *Photogramm. Eng. Remote Sens.*, **63** (1997), 691-699.
- [37] Y. Xu, Z. Wu, J. Li, A. Plaza and Z. Wei, [Anomaly detection in hyperspectral images based on low-rank and sparse representation](#), *IEEE Trans. Geosci. Remote Sens.*, **54** (2015), 1990-2000.
- [38] X. Xu and Z. Shi, [Multi-objective based spectral unmixing for hyperspectral images](#), *ISPRS-J. Photogramm. Remote Sens.*, **124** (2017), 54-69.
- [39] T. Xu, T. Z. Huang, L. J. Deng, X. L. Zhao and J. Huang, [Hyperspectral image superresolution using unidirectional total variation with Tucker decomposition](#), *IEEE J. Sel. Top. Appl. Earth Observ. Remote Sens.*, **13** (2020), 4381-4398.

- [40] N. Yokoya, T. Yairi, A. Iwasaki, X. L. Zhao and J. Huang, [Coupled nonnegative matrix factorization unmixing for hyperspectral and multispectral data fusion](#), *IEEE Trans. Geosci. Remote Sens.*, **50** (2011), 528-537.
- [41] N. Yokoya, C. Grohnfeldt and J. Chanussot, [Hyperspectral and multispectral data fusion: A comparative review of the recent literature](#), *IEEE Geosci. Remote Sens. Mag.*, **5** (2017), 29-56.
- [42] K. Zhang, M. Wang, S. Yang and L. Jiao, [Spatial-spectral-graph-regularized low-rank tensor decomposition for multispectral and hyperspectral image fusion](#), *IEEE J. Sel. Top. Appl. Earth Observ. Remote Sens.*, **11** (2018), 1030-1040.
- [43] K. Zhang, M. Wang, S. Yang, X. L. Zhao and J. Huang, [Multispectral and hyperspectral image fusion based on group spectral embedding and low-rank factorization](#), *IEEE Trans. Geosci. Remote Sens.*, **55** (2016), 1363-1371.
- [44] M. Zare, M. S. Helfroush, K. Kazemi and P. Scheunders, [Hyperspectral and multispectral image fusion using coupled non-negative Tucker tensor decomposition](#), *Remote Sens.*, **13** (2021), 2930.